Available online at www.sciencedirect.com
ScienceDirect
C. R. Chimie 10 (2007) 421–432
COMPTES RENDUS CHIMIE
http://france.elsevier.com/direct/CRAS2C/

Full paper / Mémoire

Structure–activity correlations in highly preorganized dicopper catechol oxidase model systems

Jens Ackermann [a], Silke Buchler [b], Franc Meyer [a,*]

[a] *Institut für anorganische Chemie, Georg-August-Universität Göttingen, Tammannstrasse 4, 37077 Göttingen, Germany*
[b] *Anorganisch-Chemisches Institut, Ruprecht-Karls-Universität Heidelberg, INF 270, 69120 Heidelberg, Germany*

Received 1 September 2006; accepted after revision 26 September 2006
Available online 22 December 2006

Abstract

New dicopper(II) complexes with pyrazolate-derived compartmental ligands that bear pyridyl or triazacyclononane chelate arms have been prepared and fully characterized, including several single-crystal X-ray analyses. These complexes complement a series of dicopper compounds with related pyrazolate ligands reported earlier. Modifications of the ligand scaffold are shown to control molecular features such as the Cu···Cu separation and electronic and spectroscopic properties. Catecholase activity of the new complexes has been probed using 3,5-di-*tert*-butylcatechol (DTBC) as the test substrate, revealing Michaelis–Menten-type kinetics with drastic differences in activity for the assortment of complexes. Their common skeletal motif based on the pyrazolate bridge allowed us to deduce some relationship between activity and Cu···Cu separation as well as Cu^{II}/Cu^{I} redox potentials. A dramatic effect of the buffer medium on reactivity has been observed. ***To cite this article: Jens Ackermann et al., C. R. Chimie 10 (2007).***

Keywords: Bioinorganic chemistry; Bimetallic complexes; Copper; Oxidations; Enzyme mimics

1. Introduction

Several oxidases and oxygenases contain two cooperating copper ions within their active site [1]. The two proximate metal ions serve to activate the kinetically inert O_2, and their combined redox power is used to mediate and to control the multi-electron redox reactions. Among the most prominent examples of these so-called type 3 copper centers is catechol oxidase, which catalyzes the two-electron oxidation of *ortho*-diphenols to the corresponding quinones [2]. The X-ray crystal structure analyses of catechol oxidase from sweet potatoes revealed details of the enzyme structure in different redox states and in its complex with bound inhibitor, with both copper ions found in N-donor (histidine) ligation [3]. Based on these structural findings as well as on previous spectroscopic and biochemical evidences, a plausible mechanism has been proposed for the catecholase activity [4] that includes activation of O_2 as a peroxide at the dicopper site. The two-electron substrate oxidation occurs by means of the cooperative action of the two copper ions, as each individual copper ion undergoes a one-electron redox shuttle between the +I and +II states during turnover. However, details of the mechanism are still far from clear, and several different scenarios are discussed in the literature [4–7].

* Corresponding author.
E-mail address: franc.meyer@chemie.uni-goettingen.de (F. Meyer).

1631-0748/$ - see front matter © 2006 Académie des sciences. Published by Elsevier Masson SAS. All rights reserved.
doi:10.1016/j.crci.2006.09.014

In view of the great importance of oxidation reactions for industrial and synthetic processes, and in view of the ongoing search for new and efficient oxidation catalysts, it is of paramount interest to unravel the basic functional principles that govern such bimetallic reactivity of natural enzymes and their synthetic analogues [8]. Various mono- and dinuclear copper coordination compounds have thus been investigated as biomimetic catalysts for catechol oxidation [6,9]. Parameters that determine the activity of the synthetic analogues comprise, inter alia, the metal–metal separation [10–12], the redox properties [13,14], the identity of exogenous bridging ligands [15], the structure of the dinucleating ligand scaffold [12,16,14,17], and the pH [13,18–20]. No clear relation between the catalytic activity and the redox potential of the copper species has yet emerged, which may be explained by the manifold steps that are involved in the overall catalytic cycle [21]. Dinuclear copper complexes are generally found to be more reactive than mononuclear compounds, and a steric match between the dicopper site and the substrate is assumed to be advantageous [11,12,22]. Within a series of O-atom bridged dicopper(II) complexes, those complexes with a metal–metal distance closest to that of the *met* form of the enzyme (2.9 Å) displayed the best catalytic performance [11]. In addition, some correlations between the observed rates of reactivity and ligand architecture, copper coordination environment or preorganization of the metal ions have been observed for particular classes of complexes [6]. However, a more general understanding of structure–reactivity patterns that might allow for a rational design of catalytically most active copper complexes is still lacking. Further studies of well defined and tunable dicopper complexes are obviously needed to gain deeper insight into these copper-mediated substrate oxidations and to finally unravel the parameters that determine bimetallic reactivity both in natural metalloenzymes and in small synthetic catalysts.

In this contribution we extend our investigations of the catecholase activity of highly preorganized pyrazolate-based dicopper complexes [12]. The primary intention is to elucidate trends in reactivity that might be valuable for the use of this class of complexes in oxidation catalysis in a broader sense. To this end the pyrazolate-derived compartmental ligand scaffolds offer the attractive option of targeted modulation of electronic and geometric characteristics of the bimetallic core by changes of the ligand side arms attached to the 3- and 5-positions of the heterocycle. Important variations comprise the type and number of side arm donor atoms as well as the lengths of the chelate arms. While the former allows to modify coordination numbers and electronic structures of the metal ions, the latter controls the properties of the bimetallic pocket, including the metal–metal distance [23–25].

An assortment of four dicopper complexes **1**–**4** (Scheme 1) had previously been evaluated in the catecholase reaction using 3,5-di-*tert*-butylcatechol (DTBC) as the test substrate, and drastic differences in activity became apparent from the kinetic data [12]. Among the set of complexes, those with shorter Cu···Cu distances (**1** and **2**) showed much higher activity than the systems with larger Cu···Cu separations (**3** and **4**), although other parameters are certainly relevant as well.

We now include some new dicopper(II) complexes of pyrazole-derived ligands HL^1–HL^4 that provide either pyridyl-containing or triazacyclononane (tacn) side arms (Scheme 2) [24,25]. While the metal–metal distance in **1**–**4** is controlled by the length of the spacer between the side arms N-donors, a similar effect can be achieved by modifications of the spacer between the pyrazole ring and the side arm (i.e., the ''shoulder'' of the ligand framework). For example, dinickel(II) complexes of $[L^3]^-$ and $[L^4]^-$ were shown to feature a bridging hydroxide at $d(\mathrm{Ni\cdots Ni) = 3.50}$ Å in $[L^4Ni_2(OH)]^{2+}$ versus an O_2H_3 bridge at $d(\mathrm{Ni\cdots Ni) = 4.48}$ Å in $[L^3Ni_2(O_2H_3)]^{2+}$ [24]. Both HL^3 and HL^4 can thus be expected to provide high stability constants to their dicopper complexes due to the tacn side arms, but

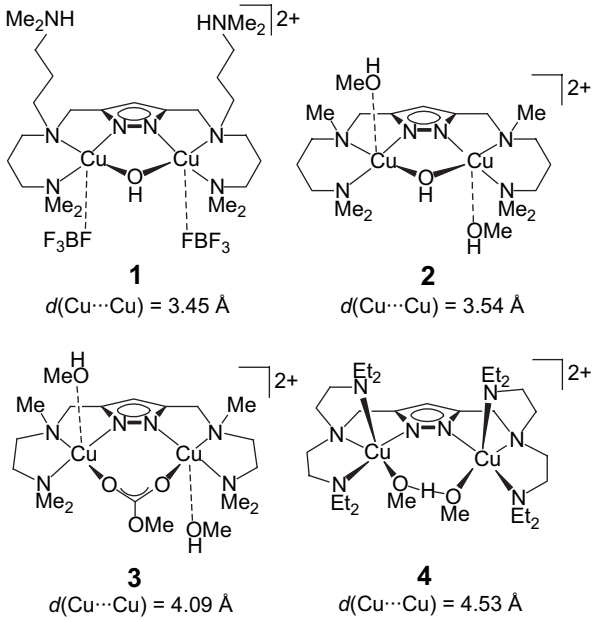

Scheme 1. Dicopper(II) complexes tested previously as functional models for the active site of catechol oxidase [12].

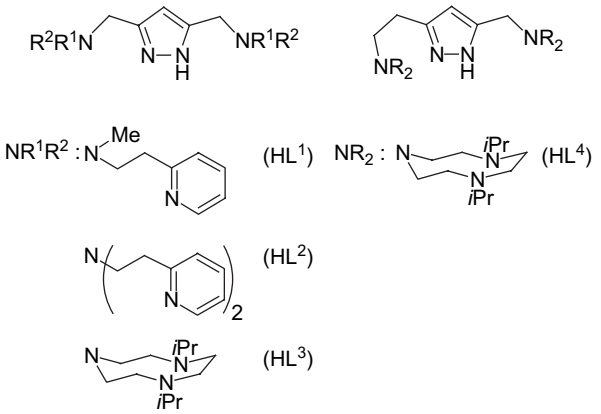

Scheme 2. Pyrazole ligands used in this work.

with very different Cu···Cu separations. At this stage of investigation the focus lies on the search for empirical structure–activity correlations, neglecting mechanistic details that most certainly are distinct for every individual system.

2. Results and discussion

2.1. Synthesis and structural characterization

Reaction of the ligand HL^1 with 1 equivalent of base (KO^tBu) and 2 equivalents of $Cu(NO_3)_2 \cdot 3H_2O$ affords complex $[L^1Cu_2(MeOH)_2(NO_3)_2]NO_3$ (**5a**). Its d–d-transition at 635 nm ($\varepsilon = 290\ mol\ l^{-1}\ cm^{-1}$) in methanol solution suggests the presence of tetragonal copper(II), which is confirmed by the single-crystal X-ray analysis. The molecular structure of the cation is depicted in Fig. 1, together with selected atom distances and bond angles. Complex **5a** contains two copper ions in distorted square-pyramidal environment ($\tau_{Cu1} = 0.11$, $\tau_{Cu2} = 0.38$)[1] [26], with the three N-atoms of the respective $[L^1]^-$ compartment and a nitrate-O forming the basal plane. A methanol ligand occupies the apical position at long (Jahn–Teller) distances of >2.2 Å, and another O-atom of the semi-chelating nitrate forms an axial contact from the backside at >2.6 Å to complete an overall {4 + 1 + 1} coordination. Interestingly, the Cu-bound methanol molecules are involved in hydrogen bonding to the nitrate-O that ligate the adjacent Cu center, which results in double (Me)O–H···O(NO_2) linkages between the two metal ions ($d_{O\cdots O} = 2.75/2.76$ Å). This arrangement forces

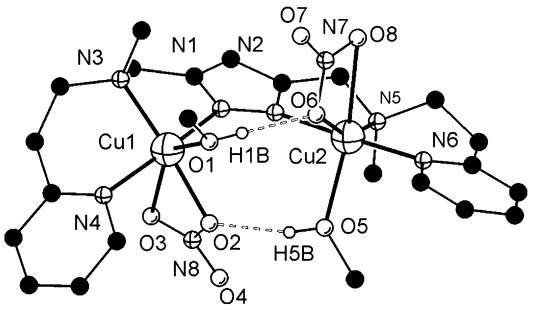

Fig. 1. Molecular structure and numbering scheme of the cationic moiety of **5a**. Most hydrogen atoms are omitted for clarity. Selected atom distances (Å) and bond angles: Cu1–N1 1.971(4) Cu1–N3 2.046(4), Cu1–N4 2.007(4), Cu1–O1 2.201(4), Cu1–O2 2.057(4), Cu1–O3 2.659(4), Cu2–N2 1.987(5), Cu2–N5 2.029(5), Cu2–N6 2.027(5), Cu2–O5 2.241(4), Cu2–O6 2.077(4), Cu2–O8 2.650(5), Cu1···Cu2 4.357(1), O1···O6 2.761(6), O5···O2 2.745(6); N1–Cu1–N3 81.1(2), N1–Cu1–N4 165.0(2), N1–Cu1–O1 100.9(2), N1–Cu1–O2 89.9(2), N3–Cu1–N4 95.2(2), N3–Cu1–O1 109.5(2), N3–Cu1–O2 158.2(2), N4–Cu1–O1 94.0(2), N4–Cu1–O2 88.4(2), O1–Cu1–O2 91.6(2), N2–Cu2–N5 82.6(2), N2–Cu2–N6 177.6(2), N2–Cu2–O5 96.6(2), N2–Cu2–O6 88.8(2), N5–Cu2–N6 95.1(2), N5–Cu2–O5 111.3(2), N5–Cu2–O6 154.5(2), N6–Cu2–O5 84.9(2), N6–Cu2–O6 93.1(2), O5–Cu2–O6 93.4(2), O1–H1B···O6 175(5), O5–H5B···O2 163(8).

the copper ions rather far apart ($d_{Cu\cdots Cu} = 4.36$ Å) and displaces them quite drastically out of the pyrazolate plane, resulting in a severe torsion Cu–N–N–Cu of 35.1°. Pyrazolate-derived ligands with long side arms that give six-membered chelate rings such as in **1**, **2**, and **5a** have been anticipated to suit well bimetallic complexes with shorter metal–metal separations of 3.5–3.9 Å, but longer separations appear to be easily accessible. Solvent insertion similar to the present case has previously been observed for dicopper(II) complexes of $[L^1]^-$ with intramolecular (H)O–H···F bridges [25]. A dominant signal in the FAB mass spectrum of **5a** at $m/z = 613$ characteristic for the ion $[L^1Cu_2(NO_3)_2]^+$ suggests, however, that the methanol molecules are readily lost under reduced pressure.

In addition to **5a**, a further complex $[L^1Cu_2F(MeOH)_2(BF_4)]BF_4$ (**5b**) with the same pyrazolate ligand was employed in this work. The molecular structure of **5b** has been determined previously [25] (Scheme 3). It also features a dicopper core based on $[L^1]^-$ with a Cu···Cu distance of around 4.3 Å (4.290(1) Å), but a single (Me)OH···F bridge is now found within the bimetallic pocket. The fluoride ion has obviously been abstracted from one of the BF_4^- counteranions. Both metal ions exhibit an almost perfect square-pyramidal coordination geometry ($\tau_{Cu1} = 0.09$, $\tau_{Cu2} = 0.01$), where the apical positions are occupied at rather long distance by either a methanol

[1] The angular structural parameter τ is defined as $\tau = (\beta - \alpha)/60$, where α and β represent two basal angles with $\beta > \alpha$. It is a measure of the degree of trigonality: a perfect TB-5 structure is associated with $\tau = 1$, while $\tau = 0$ is expected for an idealized SPY-5 geometry.

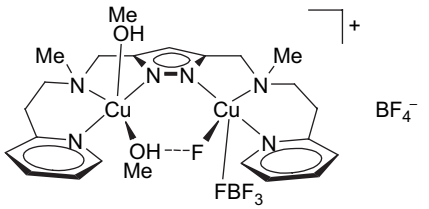

5b

Scheme 3. Complex $[L^1Cu_2F(MeOH)_2(BF_4)]BF_4$ (**5b**).

molecule ($d_{Cu2-O2} = 2.271(2)$ Å) or a fluoride atom of a BF_4^- anion ($d_{Cu1-F2} = 2.602(2)$ Å). In methanol solution, **5b** shows a visible absorption at 645 nm ($\varepsilon = 200$ mol l^{-1} cm^{-1}) in accordance with square-pyramidal coordination.

Dicopper complexes of ligand $[L^2]^-$ that contains additional donor side arms were obtained from HL^2, 2 equivalents of base (KO^tBu) and 2 equivalents of either $Cu(ClO_4)_2 \cdot 6H_2O$ or $Cu(CF_3SO_3)_2$, giving $[L^2Cu_2(OH)](ClO_4)_2$ (**6a**) or $[L^2Cu_2(OH)](CF_3SO_3)_2$ (**6b**), respectively. As shown by X-ray crystallography both complexes, **6a** and **6b**, feature very similar cations in the solid state. The molecular structure of the cation of **6b** is depicted in Fig. 2, along with selected atom distances and bond angles. Two independent but structurally similar molecules are found per unit cell.

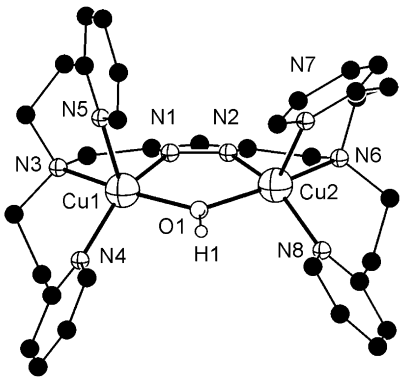

Fig. 2. Molecular structure and numbering scheme of the cationic moiety of **6b**. Most hydrogen atoms are omitted for clarity. Only one of the two crystallographically independent molecules is shown. Selected atom distances (Å) and bond angles: Cu1–N1 1.921(4), Cu1–N3 2.132(3), Cu1–N4 1.999(4), Cu1–N5 2.201(4), Cu1–O1 2.004(3), Cu2–N2 1.905(3), Cu2–N6 2.141(4), Cu2–N7 2.248(4), Cu2–N8 2.007(3), Cu2–O1 2.004(4), Cu1···Cu2 3.518(5); N1–Cu1–N3 79.4(2), N1–Cu1–N4 150.2(1), N1–Cu1–N5 101.8(2), N1–Cu1–O1 83.8(2), N3–Cu1–N4 94.9(1), N3–Cu1–N5 93.9(1), N3–Cu1–O1 161.8(1), N4–Cu1–N5 107.8(2), N4–Cu1–O1 96.2(1), N5–Cu1–O1 96.5(1), N2–Cu2–N6 78.2(1), N2–Cu2–N7 113.9(1), N2–Cu2–N8 152.2(1), N2–Cu2–O1 84.1(1), N6–Cu2–N7 92.5(1), N6–Cu2–N8 96.6(2), N6–Cu2–O1 161.0(1), N7–Cu2–N8 93.5(2), N7–Cu2–O1 101.1(1), N8–Cu2–O1 95.8(2).

Both copper ions in **6b** are hosted in their respective tetradentate binding pockets of $[L^2]^-$ and are spanned by both the pyrazolate and a hydroxide ion. Their coordination geometry can be described as distorted square-pyramidal ($\tau = 0.13-0.22$)[1] [26], with one of the pyridyl-N in the apical positions at long Cu–N distances of 2.20–2.25 Å. One of the anions (ClO_4^- for **6a**, $CF_3SO_3^-$ for **6b**) forms an O–H···O hydrogen bond with the bridging hydroxide (not shown in Fig. 2). Because of the hydroxide bridge and favored by the long ligand side arms, the Cu···Cu distance in **6a** and **6b** is relatively short (3.44–3.52 Å) and is in the range assumed to be relevant for the catechol oxidase active site. UV/vis spectra (methanol) confirm the identity of the cations of **6a** and **6b** and the preservation of the square-pyramidal coordination environment in solution ($\lambda_{max} = 645$ nm, $\varepsilon = 260$ mol l^{-1} cm^{-1}). FAB mass spectra of both complexes reveal dominant signals at $m/z = 671$ characteristic for the ion $[L^2Cu_2]^+$, suggesting that reduction to copper(I) with loss of the bridging hydroxide may readily occur under suitable conditions.

Dicopper(II) complexes of pyrazole/tacn hybrid ligands $[L^3]^-$ and $[L^4]^-$ that differ by the length of the spacer between the pyrazole and one of the tacn side arms were readily prepared from HL^3 or HL^4, 2 equivalents of base (KO^tBu) and 2 equivalents of $Cu(ClO_4)_2 \cdot 6H_2O$. Unfortunately, only $[L^3Cu_2(O_2H_3)](ClO_4)_2$ (**7**) could yet be obtained in crystalline form. The molecular structure of its cation is depicted in Fig. 3, along with selected atom distances and bond angles.

As anticipated from the constraints imposed by the ligand scaffold, **7** features a rather large Cu···Cu distance (4.41 Å) and coordination geometries of the copper ions intermediate between square-pyramidal and trigonal–bipyramidal ($\tau_{Cu1} = 0.49$, $\tau_{Cu2} = 0.50$)[1] [26]. Distortions from square-pyramidal coordination are also apparent from the band positions of the weak ligand-field transitions at 700 and 1030 nm in solution. Due to the large metal–metal separation, an additional water molecule is incorporated besides the hydroxide bridge to give a (H)O–H···O(H) unit within the bimetallic pocket. The metal ions are located almost within the plane of the pyrazolate (torsion angle Cu1–N1–N2–Cu2 of 9.7°), while the O_2H_3 bridge forms an angle of 20.7° with that plane.

The complex $[L^4Cu_2(OH)](ClO_4)_2$ (**8**) could only be obtained as a green microcrystalline powder. Its molecular structure (Scheme 4) is assumed to be similar to that of the corresponding dinickel(II) complex, which has been characterized crystallographically [24]. Due to the longer spacer between the pyrazole and one of the tacn side arms in $[L^4]^-$, the dinickel complex $[L^4Ni_2(OH)](ClO_4)_2$

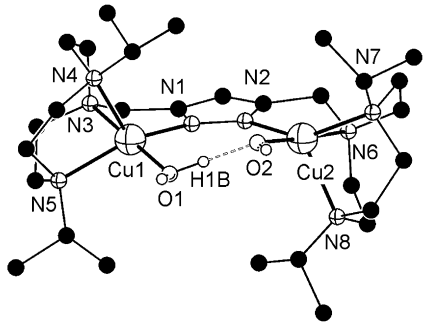

Fig. 3. Molecular structure and numbering scheme of the cationic moiety of **7**. Most hydrogen atoms are omitted for clarity. Selected atom distances (Å) and bond angles: Cu1–N1 1.998(4), Cu1–N3 2.056(4), Cu1–N4 2.206(4), Cu1–N5 2.125(4), Cu1–O1 1.905(4), Cu2–N2 2.024(4), Cu2–N6 2.048(4), Cu2–N7 2.174(4), Cu2–N8 2.200(4), Cu2–O2 1.896(4), Cu1···Cu2 4.412(1), O1···O2 2.424(6); N1–Cu1–N3 82.52(17), N1–Cu1–N4 121.13(16), N1–Cu1–N5 147.82(18), N1–Cu1–O1 95.43(17), N3–Cu1–N4 83.79(16), N3–Cu1–N5 83.15(16), N3–Cu1–O1 177.53(18), N4–Cu1–N5 85.60(16), N4–Cu1–O1 98.48(18), N5–Cu1–O1 97.97(17), N2–Cu2–N6 82.12(17), N2–Cu2–N7 146.73(16), N2–Cu2–N8 122.36(17), N2–Cu2–O2 95.42(16), N6–Cu2–N7 82.97(16), N6–Cu2–N8 84.23(17), N6–Cu2–O2 177.04(17), N7–Cu2–N8 85.33(15), N7–Cu2–O2 98.34(15), N8–Cu2–O2 98.50(17), O1–H1B···O2 168(7).

adopts a short Ni···Ni separation of 3.5 Å and hence accomodates a bridging hydroxide. A similar situation for **8** is supported by (*i*) FAB mass spectrometry showing dominant peaks at $m/z = 773$ (100% intensity) and 674 that are characteristic for ions $[L^2Cu_2(OH)(ClO_4)]^+$ and $[L^2Cu_2(OH)]^+$, respectively, and (*ii*) by the elemental analysis that is in accordance with the proposed structure. The d–d transition at 626 nm in methanol solution suggests a largely square-pyramidal coordination environment for the copper ions in **8**.

2.2. Cyclic voltammetry

Cyclic voltammetry measurements[2] reveal a first irreversible reduction process in the range −0.5 to −0.9 V for all dicopper(II) complexes **1**–**6b** with open-chain chelate arms, while reduction of complexes **7** and **8** with the pyrazole/tacn hybrid ligands takes place even below −1.0 V. The cyclic voltammogram of **5a** is shown in Fig. 4 as an example. Anodic processes only occur at high potentials. Irreversibility of the reduction had to be expected because of the drastic differences in stereoelectronic requirements for copper(II) and copper(I). Generation of copper(I) is probably accompanied by rapid dissociation of the secondary bridging units, i.e., OH or (R)O–H···O(R), which are known to

[2] All values versus the Cp_2Fe/Cp_2Fe^+ couple.

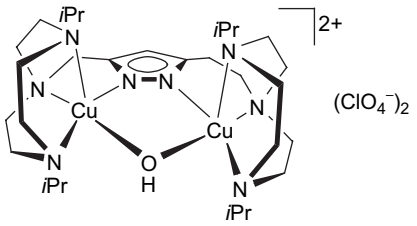

Scheme 4. Proposed structure of $[L^4Cu_2(OH)](ClO_4)_2$ (**8**).

have a poor binding ability to copper(I) ions. However, irreversibility of the electrochemical redox processes does by no means preclude the suitability of the respective complexes as oxidation catalysts. The only crucial condition in this respect is that they can be reoxidized at appropriate potentials. According to previous work the redox potentials have to be in a suitable window for facile reduction of the catechol substrate on the one hand and the subsequent re-oxidation of the complex by molecular oxygen on the other hand [14,21]. It should be mentioned, however, that most previous investigations did not show a clear relation between the catalyst's redox potential and the catalytic activity [6].

Even though the irreversibility of the electrochemical redox processes hampered their comparison for the various complexes, the present set of systems can be ranked qualitatively by their E_p^{Red} values obtained under similar conditions (Table 1). While comparable values of −0.75, −0.68 and −0.76 V were found for **1**, **2** and **3**, complex **4** exhibits greater stabilization of the copper(II) form as indicated by $E_p^{Red} = -0.90$ V. This is in line with the relatively low catecholase

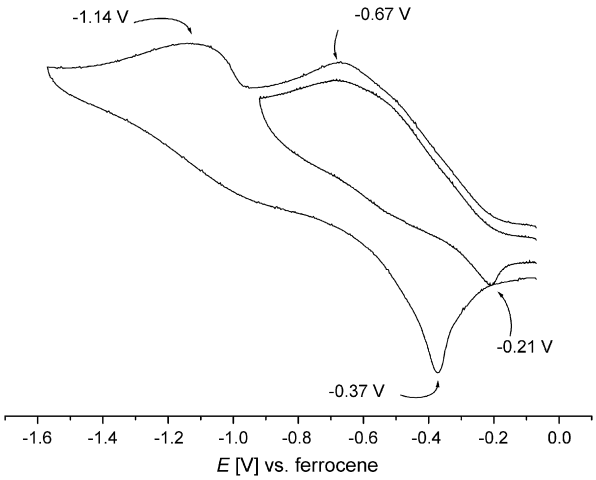

Fig. 4. Cyclic voltammogram of **5a** in acetonitrile (0.1 M $N^nBu_4PF_6$, 100 mV s^{-1}); peak potentials in volts versus the Cp_2Fe^+/Cp_2Fe couple.

Table 1
Electrochemical properties of the complexes in acetonitrile[a]

Complex	$E_p^{Red,1}$ [V]	$E_p^{Red,2}$ [V]
1	−0.75	–
2	−0.68	−1.08
3	−0.76	−1.03
4	−0.90	–
5a	−0.67	−1.14
6b	−0.53	−1.11
7	−1.07	–
8	−1.38	–

[a] $N^nBu_4PF_6$ (0.1 M), 200 mV s^{-1} for **1**–**4**, 100 mV s^{-1} for **5a**, **6b**, **7**, and **8**; peak potentials in volts versus the Cp_2Fe^+/Cp_2Fe couple.

activity of this complex [12]. Among the new dicopper complexes reported here, complex **6b** features the highest E_p^{Red} of −0.53 V, while the value for **5a** is close to those of **1**–**3**. The structural rigidity of the tacn ligand side arms in **7** and **8** is not suited to adapt to the very different stereoelectronic requirements of Cu^I and Cu^{II}, and hence these complexes have the lowest E_p^{Red} values.

2.3. Catecholase activity

Catecholase activities of complexes **5a**, **5b**, **6b**, **7**, and **8** were probed with the commonly used DTBC as a test substrate. The low redox potential of DTBC makes it easy to oxidize, and its bulky *tert*-butyl groups prevent unwanted side reactions such as ring opening or polymerization of the resulting quinone. The oxidation product 3,5-di-*tert*-butyl-*o*-quinone (DTBQ) displays a strong absorption at $\lambda_{max} = 400$ nm whose appearance can be conveniently followed by UV/vis spectroscopy. Kinetics of the catecholase reactions mediated by the various dicopper complexes were analyzed by the initial rate method.

Exploratory experiments in methanol solution at 20 °C revealed only negligible activity of **8** and very low activity of **7** ($k_{exp} = 2.2 \pm 0.2\ h^{-1}$; $v_0 = k_{exp} \cdot [complex]$). A slight increase in activity for **8** could be observed when the reaction was carried out in a mixture of methanol and aqueous TRIS buffer (29:1) at pH 8 and 40 °C.[3] First-order dependence of the initial rate on catalyst concentration ($k_{exp} = 2.8 \pm 0.1\ h^{-1}$) as well as saturation kinetics at high concentrations of the substrate was found under those conditions. Interpretation of the experimental data on the basis of a Michaelis–Menten model, originally developed for enzyme kinetics, gave the following parameters: $k_{cat} = 3.9 \pm 0.4\ h^{-1}$, $K_M = (1.8 \pm 0.1) \times 10^{-3}$ mol l^{-1}, and $v_{max} = (8.1 \pm 0.8) \times 10^{-6}$ mol l^{-1} min^{-1} (determined from a Lineweaver–Burk plot). Due to their low activities, complexes **7** and **8** were not investigated in greater detail.

[3] For these experiments, TRIS buffer was used as the NO_3^- salt.

Table 2
Kinetic parameters of the oxidation of DTBC by the catalysts **5a**, **5b**, and **6b**[a]

	k_{exp} [h^{-1}]	k_{cat} [h^{-1}]	K_M [mol l^{-1}]	v_{max} [mol l^{-1} min^{-1}]
5a[b]	593 ± 4	1125 ± 102	$(1.0 \pm 0.1) \times 10^{-3}$	$(3.8 \pm 0.3) \times 10^{-4}$
5b[b]	629 ± 12	1432 ± 93	$(1.4 \pm 0.1) \times 10^{-3}$	$(4.8 \pm 0.3) \times 10^{-4}$
6b[c]	5178 ± 62	6502 ± 239	$(7.5 \pm 0.5) \times 10^{-4}$	$(10.8 \pm 0.3) \times 10^{-4}$

[a] At 20 °C in a mixture of methanol and 0.27 M aqueous TRIS buffer (29:1), v_{max} was obtained from the Lineweaver–Burk plot.
[b] pH 7.3.
[c] pH 8.0.

Complexes **5a**, **5b**, and **6** exhibit much higher activities in the same mixture of methanol and aqueous TRIS buffer (29:1) even at 20 °C. Since $[L^1]^-$ with its few long chelate arms imparts relatively low stability to its dicopper complexes at higher pH, catecholase experiments were conducted at pH 7.3 for **5a**,**b**. A linear dependence of the initial rate on catalyst concentration was found when the concentration was varied between 10^{-5} and 10^{-4} M (**5a**,**b**) or 10^{-6} and 10^{-5} M (**6b**) while $[DTBC]_0$ was kept constant at a large initial excess of 2×10^{-3} M.[4] Complexes **5a** and **5b** show an almost identical catalytic behavior with pseudo first-order rate constants $k_{exp} = 593 \pm 4\ h^{-1}$ (**5a**) and $629 \pm 12\ h^{-1}$ (**5b**) (Table 2), which suggests that the different moieties within the bimetallic pocket (double (Me)O–H···O(NO_2) bridges in **5a** versus (Me)O–H···F bridge in **5b**) are rapidly displaced under the experimental conditions to give the same species in solution. This is corroborated by comparison of the UV/vis spectra of **5a**,**b** in methanol and in methanol/TRIS buffer (29:1)[3] (Fig. 5). In pure methanol, both λ_{max} values and intensities of the d–d absorption bands for **5a** and **5b** are clearly different, while their spectra are basically identical in TRIS buffered solution. ESI mass spectrometric results for the different solutions are in accordance with the conclusions drawn from the UV/vis data: while a signal at $m/z = 508$ for $[L^5Cu_2F]^+$ confirms the presence of the fluoride ligand for **5b** in pure methanol, no such signal can be detected in TRIS buffered solution. In the latter medium, spectra for **5a** and **5b** are almost identical and show peaks at $m/z = 489$ for the fragment $[L^5Cu_2]^+$ and at $m/z = 613$ characteristic for $[L^5Cu_2(NO_3)_2]^+$ (note that TRIS buffer was used as the NO_3^- salt in these experiments).

[4] The relationship between v_0 and catalyst concentration is not strictly linear at higher catalyst concentrations, suggesting a more complex situation that may also involve oligomeric species.

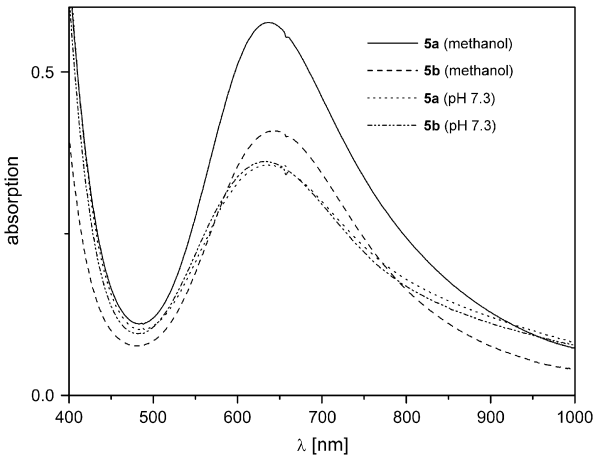

Fig. 5. UV/vis spectra of **5a**,**b** in pure methanol and in methanol/TRIS buffer (29:1) at pH 7.3.

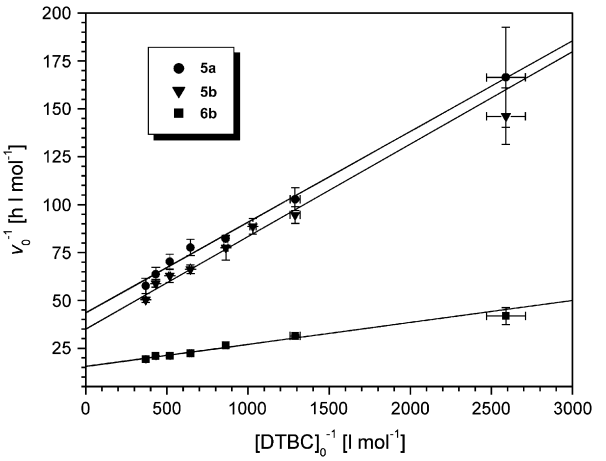

Fig. 6. Lineweaver–Burk plots for the catalysts **5a**, **5b** (at pH 7.3) and **6b** (at pH 8); $[\mathbf{5a}]_0 = [\mathbf{5b}]_0 = 2 \times 10^{-5}$ M, $[\mathbf{6b}]_0 = 10^{-5}$ M; $T = 20\,^{\circ}$C.

A linear relationship between initial rates and catalyst concentrations was also found for **6b**. The catalytic activity of **6b** is the highest among all pyrazolate-based dicopper complexes examined so far ($k_{exp} = 5178 \pm 62$ h^{-1} at pH 8.0, Table 2). Saturation kinetics were observed for all complexes **5a**,**b** and **6b** when the substrate concentration $[DTBC]_0$ was varied between 4×10^{-4} and 2.8×10^{-3} M while the catalyst concentration was kept constant at 2×10^{-5} (for **5a**,**b**) or 10^{-5} M (for **6b**). Lineweaver–Burk plots are shown in Fig. 6, and data derived from the Michaelis–Menten model are given in Table 2.

2.4. Structure–activity correlations

The various catechol oxidase model systems **1**–**8** have as a common structural motif the pyrazolate bridge spanning the two metals, while differences are introduced via the chelating N-donor side arms that generate distinct binding sites for hosting the proximate copper ions. Given this structural relationship, comparison of the available data for the series of catalysts allows to establish some qualitative structure–activity correlations, even though kinetic data have been obtained under somewhat distinct conditions that proved most appropriate for the individual systems. In Fig. 7 the experimental pseudo first-order rate constants k_{exp} are plotted versus the Cu···Cu separation of the bimetallic core as determined by X-ray crystallography. The ligand scaffolds certainly provide some structural flexibility, and the Cu···Cu distances observed for the solid state may differ to a certain extent in solution. However, the length and topology of the ligand side arms constrains the accessible range of metal–metal distances, and as a general trend it is clearly discernible that shorter Cu···Cu distances are advantageous for high catecholase activity.

On the other hand, complex **8** that is believed to feature a very short Cu···Cu distance (as concluded from the structure of the corresponding dinickel analogue) exhibits extremely low activity, indicating that additional factors play a decisive role. Fig. 8 illustrates the relation between k_{exp} and the redox properties (qualitatively expressed by the E_p^{Red} values). It is quite evident that all dicopper catalysts with E_p^{Red} below a threshold value of around −0.8 V are barely active. In the same tenor one may argue that the activity of **6b** is highest because of its favorable combination of short Cu···Cu separation and comparatively high redox potential. It has to be emphasized, however, that the present

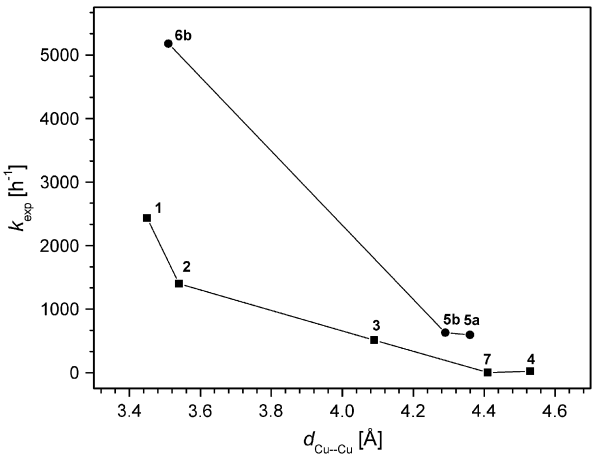

Fig. 7. Catecholase activity versus Cu···Cu distance for the pyrazolate-based catalysts.

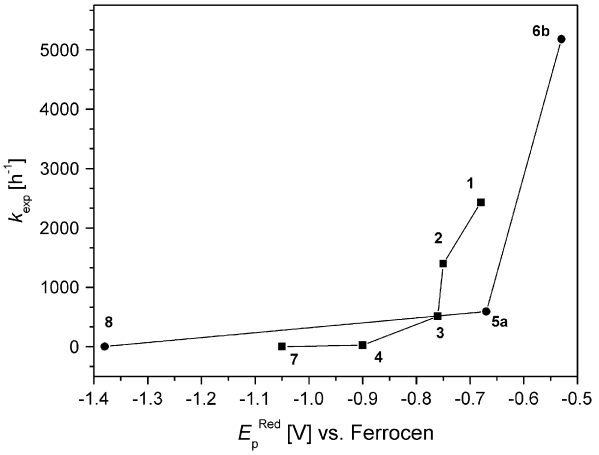

Fig. 8. Catecholase activity and reduction peak potentials (E_p^{Red} values versus Cp_2Fe^+/Cp_2Fe).

structure–activity correlations are purely empirical and are not founded on any detailed mechanistic basis.

In view of the very high activity of **6b**, the influence of pH was investigated in some more detail for this particular catalyst system. The AcOH/AcO$^-$, MES, MOPS, and TRIS buffers were used to cover different pH ranges, and results are summarized in Fig. 9. It is apparent that the type of buffer has a dramatic effect on the catecholase activity. While the sluggish reactivity at low pH may be explained by protonation of the bridging hydroxide and/or inhibition by the acetate anion, the negligible reactivity in MEPS or MOPS buffered solution (pH 5.6–7.6) is unexpected and suggests some undesired interaction between the buffer and the catalyst. In contrast, use of either nitrate or chloride in the case of TRIS buffer has only a minor effect. Somewhat lower activities around the optimum pH 8.0 may

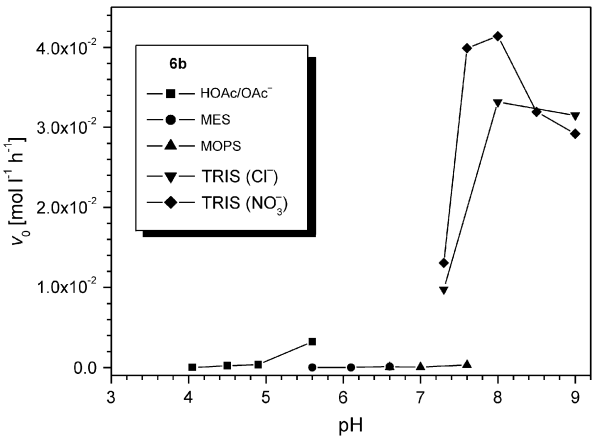

Fig. 9. Effect of pH and buffer on the catecholase activity (initial rates v_0) of **6b**.

again suggest competitive inhibition by the chloride, and in line with this assumption a Cl-bridged complex $[L^2Cu_2Cl](CF_3SO_3)_2$ (**9**) could be isolated in independent experiments and structurally characterized (Fig. 10). In complex **9** the chloride ion blocks the binding site within the bimetallic pocket at a Cu···Cu separation of 3.83 Å.

The catecholase activity of simple Cu^{2+} salts such as copper(II) nitrate, tetrafluoroborate, or triflate in TRIS buffer at pH 8.0 is much lower than the activity of **6b**, which ascertains that TRIS does not extract the metal ions from the complex. Integrity of **6b** under these conditions is confirmed by UV/vis spectroscopy. While at present the reason for the dramatic effect of the buffer remains unknown, it is obvious that great caution has to be exercised when comparing catalytic data from different studies employing different solvents and buffers.

3. Concluding remarks

A set of four new dicopper complexes with different pyrazolate-based compartmental ligands has been prepared and complements a series of related dicopper systems reported earlier. The thus available assortment of complexes featuring a common structural motif provides a suitable basis for establishing some qualitative structure–activity correlations. Distinctions between

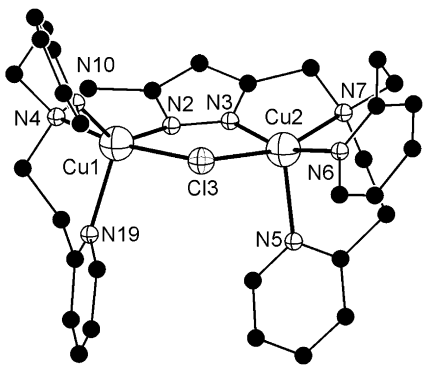

Fig. 10. Molecular structure and numbering scheme of the cationic moiety of **9**. Hydrogen atoms are omitted for clarity. Selected atom distances (Å) and bond angles: Cu1–N2 1.932(3), Cu1–N4 2.115(3), Cu1–N10 2.044(3), Cu1–N19 2.179(4), Cu1–Cl3 2.440(1), Cu2–N3 1.900(3), Cu2–N5 2.207(4), Cu2–N6 1.980(3), Cu2–N7 2.158(4), Cu2–Cl3 2.412(1), Cu1···Cu2 3.829(2); N2–Cu1–N4 81.5(1), N2–Cu1–N10 139.4(1), N2–Cu1–N19 111.6(1), N2–Cu1–Cl3 86.9(1), N4–Cu1–N10 96.0(1), N4–Cu1–N19 94.1(1), N4–Cu1–Cl3 167.3(1), N10–Cu1–N19 109.0(1), N10–Cu1–Cl3 89.5(1), N19–Cu1–Cl3 95.0(1), N3–Cu2–N5 102.0(1), N3–Cu2–N6 160.6(1), N3–Cu2–N7 80.0(2), N3–Cu2–Cl3 87.2(1), N5–Cu2–N6 97.2(1), N5–Cu2–N7 96.8(2), N5–Cu2–Cl3 99.0(1), N6–Cu2–N7 95.0(2), N6–Cu2–Cl3 92.6(1), N7–Cu2–Cl3 161.4(1).

the various complexes are introduced by different chelate side arms of the ligand scaffolds, imparting different Cu···Cu distances and redox potentials. This leads to greatly differing activities in the catalytic oxidation of DTBC mediated by those complexes. All complexes investigated here (and most of the other pyrazolate-bridged complexes investigated earlier [12]) display a Michaelis–Menten type kinetic behavior, although detailed mechanistic information is not yet available for the individual catalysts. Caution is thus recommended when comparing and interpreting relative activities, but nevertheless some empirical relationships between molecular structure and reactivity are discernible from the present work. Here it is apparent that both Cu···Cu separation and redox potential play an important role: the shortest Cu···Cu distance accessible with the present set of systems (~3.5 Å) is clearly advantageous for high activity (which decreases at larger distances), and activity is greatly diminished when the dicopper complex has a redox potential below a certain threshold value (qualitatively expressed here by an E_p^{Red} value of −0.8 V). Both parameters have to be considered simultaneously, and it is likely that additional factors play a role as well. Finally one should be very cautious when comparing activity data from different studies that use different solvents and buffers, since a dramatic effect of the buffer on activity is possible, as observed here for the most active complex **6b**.

4. Experimental

4.1. General procedures and methods

HL^1, HL^2, HL^3, and HL^4 were prepared as described previously [24,25]. Solvents were dried according to established procedures and distilled prior to be used. All other chemicals were purchased from commercial sources and used as received. Yields of crystalline complexes given in the experimental procedures are not optimized. Microanalyses: Analytical Laboratory of the Institute of Inorganic Chemistry at Georg-August-University Göttingen. IR spectra: Digilab Excalibur, recorded as KBr pellets. Wavelengths in cm^{-1}. UV/vis spectra: Varian Cary 1E or Cary-5000, measured in quartz cuvettes of 0.2 cm or 1 cm path length. Wavelengths λ in nm and extinction coefficients ε in $l\,mol^{-1}\,cm^{-1}$. Mass spectra: Finnigan MAT 95 (FAB-MS). Cyclic voltammetry: Perkin–Elmer Model 263A instrument with glassy-carbon working electrode and platinum reference and counter electrodes, in 0.1 M $N^nBu_4PF_6/CH_3CN$. Ferrocene (the potential being 0.45 V versus SCE in DMF) was used as internal standard.

4.2. Syntheses of the complexes

4.2.1. $[L^1Cu_2(MeOH)_2(NO_3)_2]NO_3$ (**5a**)

To a solution of HL^1 (295 mg, 0.81 mmol) in 150 ml methanol were added 1 equivalent of KO^tBu (91 mg, 0.81 mmol) and 2 equivalents of $Cu(NO_3)_2\cdot 3H_2O$ (391 mg, 1.62 mmol) and the reaction mixture was stirred for 2 h. After removal of all volatile material under reduced pressure the residue was redissolved in a small amount of methanol, filtered, and the solution layered with Et_2O to gradually afford blue crystals of the product **5a**. Yield: 330 mg (0.45 mmol, 56%); IR (KBr): $\tilde{\nu} = 3365$(m), 2931(m), 2876(m), 2486(w), 2397(w), 1764(w), 1611(s), 1570(m), 1484(s), 1437(s), 1384(s), 1357(s), 1286(s), 1160(m), 1105(m), 1062(w), 1012(m), 979(w), 959(w), 911(w), 841(w), 825(w), 812(w), 769(m), 709(w), 649(w), 590(w), 537(w), 472(w), 429(w), 317(w); MS (FAB, Nibeol): m/z (%) = 613 (100, $[L^1Cu_2(NO_3)_2]^+$), 551 (66, $[L^1Cu_2(NO_3)]^+$), 489 (32, $[L^5Cu_2]^+$), 355 (70, $[L^1Cu_2 - MeN(CH_2CH_2py) + 1]^+$), 291 (39, $[L^1Cu - MeN(CH_2CH_2py]^+$); UV/vis (MeOH): λ (ε) = 216 (26 600), 259 (16 010), 284 (sh, 7190), 635 (290); elemental analysis [%] calcd for $C_{23}H_{35}Cu_2N_9O_{11}$ (740.67 g/mol): C 37.30, H 4.76, N 17.02; found C 37.06, H 4.98, N 17.05.

4.2.2. $[L^2Cu_2(OH)](ClO_4)_2$ (**6a**)

To a solution of HL^2 (120 mg, 0.23 mmol) in acetonitrile (150 ml) were added 1.9 equivalents of KO^tBu (49 mg, 0.44 mmol) and 1.9 equivalents of $Cu(ClO_4)_2\cdot 6H_2O$ (163 mg, 0.44 mmol) and the dark green reaction mixture was stirred for 6 h. After removal of all volatile material under reduced pressure the residue was redissolved in a small amount of dichloromethane, filtered, and the solution layered with pentane and stored at 4 °C to gradually afford green crystals of $\mathbf{6a}\cdot 2CH_2Cl_2$. Yield: 67 mg (0.08 mmol, 33%); IR (KBr): $\tilde{\nu} = 3524$(m), 3443(m), 3076(w), 2959(w), 2923(w), 2867(w), 1606(s), 1569(m), 1487(m), 1443(s), 1309(w), 1091(vs), 768(s), 622(s); MS (FAB, nibeol): m/z (%) = 770 (27, $[L^2Cu_2(ClO_4)]^+$), 671 (100, $[L^2Cu_2]^+$], 607 (20, $[L^2Cu]^+$], 564 (18, $[L^2Cu_2 - CH_3CH_2py]^+$), 382 (63, $[L^2Cu - N(CH_2CH_2py)_2]^+$); UV/vis (MeOH): λ (ε) = 234 (18 200), 257 (21 820), 644 (270); elemental analysis [%] calcd for $C_{33}H_{38}Cu_2Cl_2N_8O_4$ (888.70 g/mol): C 44.60, H 4.31, N 12.61; found C 46.05, H 4.59, N 13.02.

4.2.3. $[L^2Cu_2(OH)](CF_3SO_3)_2$ (**6b**)

To a solution of HL^2 (285 mg, 0.55 mmol) in methanol (150 ml) were added 1.9 equivalents of KO^tBu (117 mg, 1.04 mmol) and 1.9 equivalents of $Cu(CF_3SO_3)_2$ (377 mg,

1.04 mmol) and the reaction mixture was stirred for 2 h. After removal of all volatile material under reduced pressure the residue was redissolved in a small amount of acetone, filtered, and the solution layered with pentane to gradually afford green crystals of **6b**·acetone. Yield: 83 mg (0.08 mmol, 15%); IR (KBr): $\tilde{\nu} = 3546$(w), 3075(w), 2964(s), 2907(w), 2861(w), 1662(w), 1645(w), 1571(w), 1488(w), 1445(w), 1417(w), 1262 (s), 1224(w), 1098(s), 1030(s), 864(w), 801(s), 699(w), 637(m), 573(w), 517(w), 394(m); MS (FAB, nibeol): *m/z* (%) = 988 (2, $[L^2Cu_2(OH)(CF_3SO_3)_2]^+$), 972 (24, $[L^2Cu_2(CF_3SO_3)_2]^+$), 822 (59, $[L^2Cu_2(CF_3SO_3)]^+$), 671 (100, $[L^2Cu_2]^+$), 564 (17, $[L^2Cu_2 - CH_3CH_2py]^+$), 382 (32, $[L^2Cu - N(CH_2CH_2py)_2]^+$); UV/vis (MeOH): λ (ε) = 206 (19 050), 221 (sh, 15 940), 258 (16 870), 648 (250); elemental analysis [%] calcd for $C_{35}H_{38}Cu_2F_6N_8O_7S_2$·acetone (1040.79 g/mol): C 43.63, H 4.24, N 10.90; found C 43.30, H 4.22, N 10.92.

4.2.4. $[L^3Cu_2(O_2H_3)](ClO_4)_2$ (7)

To a solution of HL^3 (177 mg, 0.34 mmol) in ethanol (70 ml) were added 2 equivalents of KO^{t}Bu (77 mg, 0.68 mmol) and 2 equivalents of $Cu(ClO_4)_2 \cdot 6H_2O$ (253 mg; 0.68 mmol) and the reaction mixture was stirred for 12 h and then filtered. After removal of all volatile material under reduced pressure, the resulting residue was redissolved in a small amount of acetone and layered with Et_2O to gradually afford green crystals of the product **7**·acetone. Yield: 222 mg (0.24 mmol, 70%); IR (KBr): $\tilde{\nu} = 3439$(m), 2966(m), 1700(m), 1625(m), 1586(m), 1490(m), 1453(m), 1384(m), 1372(m), 1350(w), 1327(w), 159(w), 1094(vs), 950(w), 794(m), 735(m), 713(m), 622(s); MS (FAB, nibeol): *m/z* (%) = 761 (15, $[L^3Cu_2(OH)(ClO_4)]^+$), 744 (10, $[L^3Cu_2(ClO_4)]^+$), 660 (15, $[L^3Cu_2(OH)]^+$), 643 (35, $[L^3Cu_2]^+$), 368 (100, $[L^3Cu - C_{12}H_{26}N_3]^+$); UV/vis (MeOH): λ (ε) = 700 (126), 1030 (43); elemental analysis [%] calcd for $C_{29}H_{60}N_8Cu_2O_{10}Cl_2$·acetone (936.91 g/mol): C 41.02, H 7.10, N 11.96; found C 40.88, H 7.00, N 11.96.

4.2.5. $[L^4Cu_2(OH)](ClO_4)_2$ (8)

To a solution of HL^4 (205 mg, 0.38 mmol) in methanol (150 ml) were added 2 equivalents of KO^{t}Bu (85 mg, 0.76 mmol) and 2 equivalents of $Cu(ClO_4)_2 \cdot 6H_2O$ (282 mg, 0.76 mmol) and the green reaction mixture was stirred for 12 h. After removal of all volatile material under reduced pressure, the resulting residue was redissolved in a small amount of acetone, filtered, and layered with pentane. The product **8** gradually precipitated as a green powder which was isolated by filtration and dried under reduced pressure. Non-optimized yield: 110 mg (0.13 mmol, 34%); IR (KBr): $\tilde{\nu} = 3600$(m), 2970(s), 2942(s), 2862(m), 1710(m), 1495(m), 1463(m), 1389(m), 1372(m), 1330(m), 1293(w), 1226(w), 1093(vs), 1024(m), 967(m), 806(m), 769(m), 715(m), 623(s), 458(m); MS (FAB, nibeol): *m/z* (%) = 773 (100, $[L^4Cu_2(OH)(ClO_4)]^+$), 674 (44, $[L^4Cu_2(OH)]^+$), 657 (20, $[L^4Cu_2]^+$); UV/vis (MeOH): λ (ε) = 210 (7920), 267 (6900), 325 (sh, 3180), 375 (3150), 626 (230); elemental analysis [%] calcd for $C_{30}H_{60}Cl_2Cu_2N_8O_9$ (847.83 g/mol): C 41.19, H 6.91, N 12.81; found C 41.26, H 6.97, N 12.62.

4.2.6. $[L^2Cu_2Cl](CF_3SO_3)_2$ (9)

To a solution of HL^2 (399 mg, 0.73 mmol) in dichloromethane (150 ml) were added 2.0 equivalents of KO^{t}Bu (164 mg, 1.46 mmol) and 2.0 equivalents of $Cu(CF_3SO_3)_2$ (528 mg, 1.46 mmol) and the dark green reaction mixture was stirred for 6 h. After removal of all volatile material under reduced pressure the residue was redissolved in a small amount of dichloromethane, filtered, and the solution layered with diethyl ether to gradually afford green crystals of **9**·CH_2Cl_2. Yield: 205 mg (0.19 mmol, 26%); IR (KBr): $\tilde{\nu} = 3084$(w), 2953(w), 2921(w), 2871(w), 1610(s), 1571(m), 1488(m), 1447(s), 1276(s), 1224(s), 1155(s), 1109(m), 1058(w), 1030(s), 957(w), 932(w), 837(w), 786(m), 770(s), 731(w), 699(w), 637(s), 573(m), 516(s); MS (ESI, MeOH): *m/z* (%) = 879 (100, $[L^2Cu_2Cl(CF_3SO_3)Na]^+$), 865 (40), 857 (35, $[L^2Cu_2Cl(CF_3SO_3)]^+$); UV/vis (MeOH): λ (ε) = 210 (17 800), 221 (sh, 17 330), 259 (19 780), 652 (270); elemental analysis [%] calcd for $C_{35}H_{37}Cu_2ClF_6N_8O_6S_2 \cdot CH_2Cl_2$ (1091.32 g/mol): C 39.62, H 3.60, N 10.27; found C 39.14, H 3.71, N 10.27.

4.3. Kinetic measurements

These were carried out at 20 °C in a thermostated quartz cell ($d = 1$ cm) with magnetic stirrer using a mixture of methanol and 0.27 M aqueous TRIS buffer (29:1) at pH 7.3 (for **5a**,**b**) or pH 8.0 (for **6b**). The increase of the absorption band of the product DTBQ at 400 nm ($\varepsilon = 1810\ l\ mol^{-1}\ cm^{-1}$) was followed by UV/vis spectroscopy. Each experiment was performed at least three times, and the obtained plots were analyzed by the initial rate method. In a first test series, solutions with varying complex concentration in the range 9.7×10^{-6}–9.7×10^{-5} M (**5a**,**b**) or 9.7×10^{-7}–9.7×10^{-6} M (**6b**) were prepared while the concentration of DTBC was kept constant (1.9×10^{-3} M). In a second test series, the complex concentrations were held constant at 1.9×10^{-5} M (**5a**,**b**) or 10^{-5} M (**6b**)

while the catechol concentration was varied in the range 3.9×10^{-4}–2.7×10^{-3} M. The rate law dependence on complex concentration was found to be first order while saturation kinetics were observed for the dependence on substrate concentration. A Michaelis–Menten analysis of the data was applied and v_{max}, K_M and k_{cat} determined from a Lineweaver–Burk plot. All errors were calculated conservatively. Blank experiments were carried out with simple copper(II) salts such as $Cu(ClO_4)_2 \cdot 6H_2O$, $Cu(BF_4)_2 \cdot 6H_2O$, or $Cu(NO_3)_2 \cdot 3H_2O$ under identical conditions, and the observed catalytic activities of these salts were generally much lower than those of the dinuclear complexes with the respective anion.

4.4. Test for H_2O_2

First the DTBC was oxidized in the presence of the respective catalyst and air until an absorption $A_{400} = 0.4$ was reached. The reaction was then quenched with the same volume of 0.005 M H_2SO_4 and the product DTBQ as well as residual DTBC removed by extraction with CH_2Cl_2. To 2 ml of the remaining solution was added 1 ml of H_2O in the reference cell. In the other cell 1 ml of a 0.3 M KI solution and catalytic amounts of lactoperoxidase for specific acceleration of the oxidation of I^- to I_3^- were added. The development of the absorption band A_{353} ($\varepsilon = 26\,000$ mol l^{-1} cm^{-1}) of the resulting I_3^- was followed by UV/vis spectroscopy. In a blank experiment the same procedure was followed for a reaction mixture containing the catalyst, but no substrate. Additionally, each measurement was verified by H_2O_2 test strips from Merck. Both tests were negative for all examined catalysts.

4.5. X-ray crystallography

X-ray data were collected on a Stoe IPDS II diffractometer (**5a**), a four-circle diffractometer with Offset-Euler balance with a Bruker SMART 4K CCD-counter diffractometer (**6a**, **6b**), a Nonius Kappa CCD diffractometer (**7**) using graphite monochromated Mo Kα radiation ($\lambda = 0.71073$ Å), and a Bruker SMART 6000 4K CCD diffractometer (**9**) using monochromated Cu Kα radiation ($\lambda = 1.54178$ Å) (Table 3). The structures were solved by direct methods and refined on F^2 using all reflections with SHELX-97 [27]. Atomic coordinates and thermal parameters of the non-hydrogen atoms were refined in fully anisotropic models. Hydrogen atoms were either located in the difference Fourier map and refined isotropically or included using the riding model. SADABS was used to perform area-detector scaling and absorption corrections for **6a** ($T_{max/min} = 1/$

Table 3
Crystal data and refinement details for **5a**, **6a**, **6b**, **7**, and **9**

	5a	**6a**	**6b**	**7**	**9**
Empirical formula	$[C_{23}H_{35}Cu_2N_8O_8]^+NO_3^-$	$[C_{33}H_{38}Cu_2N_8O]^{2+}$ $2ClO_4^- \cdot 2CH_2Cl_2$	$[C_{33}H_{38}Cu_2N_8O]^{2+}$ $2CF_3O_3S^- \cdot C_3H_6O$	$[C_{32}H_{66}Cu_2N_8O_2]^{2+}$ $2ClO_4^- \cdot C_3H_6O$	$[C_{33}H_{37}ClCu_2N_8]^{2+}$ $2CF_3O_3S^- \cdot CH_2Cl_2$
Formula weight	740.68	1058.55	1046.03	936.91	1091.32
Crystal size [mm]	0.30 × 0.20 × 0.20	0.43 × 0.39 × 0.11	0.41 × 0.32 × 0.21	0.15 × 0.10 × 0.05	0.60 × 0.45 × 0.34
T [K]	133	190	133	200	277
Crystal system	Triclinic	Monoclinic	Orthorhombic	Orthorhombic	Monoclinic
Space group	P-1 (no. 2)	$P2_1/n$ (no. 14)	$Pna2_1$ (no. 33)	$P2_12_12$ (no. 18)	$P2_1/n$ (no. 14)
a [Å], α [°]	8.382(2), 62.94(3)	9.0111(8), 90	22.552(14), 90	17.540(4), 90	21.609(4), 90
b [Å], β [°]	13.924(3), 83.62(3)	39.929(3), 106.223(2)	13.21(2), 90	24.287(5), 90	13.260(3), 107.21(3)
c [Å], γ [°]	14.606(3), 85.64(3)	12.1896(10), 90	28.35(5), 90	9.955(2), 90	16.663(3), 90
V [Å^3]	1508.1(5)	4211.2(6)	8449(21)	4240.8(15)	4560.9(16)
$\rho_{calcd.}$ [g cm^{-3}]	1.631	1.670	1.636	1.467	1.586
Z	2	4	8	4	4
$F(000)$	764	2160	4268	1976	2208
μ [mm^{-1}]	1.483	1.454	1.193	1.192	4.302
hkl range	±9, ±16, −14 to 17	−12–11, 0–53, 0–16	−29–18, ±17, ±36	±22, −31–30, ±12	−23–24, ±14, ±18
θ range [°]	2.45–24.63	2.81–28.70	1.79–27.59	1.43–27.00	2.14–59.97
Measured refl.	12 347	29 282	125 703	9705	28 340
Unique refl. [R_{int}]	5049 [0.0952]	10 802 [0.0430]	19 490 [0.0705]	9246 [0]	6582 [0.0231]
Observed refl. $I > 2\sigma$ (I)	3690	8292	16 630	7091	6273
Refined parameters	409	701	1164	519	579
Goodness-of-fit	0.983	1.067	1.071	1.120	1.060
$R1$, $wR2$ ($I > 2\sigma$ (I))	0.0597, 0.1409	0.0501, 0.1098	0.0459, 0.0931	0.0730, 0.1008	0.0606, 0.1773
$R1$, $wR2$ (all data)	0.0819, 0.1507	0.0704, 0.1193	0.0605, 0.0997	0.1070, 0.1094	0.0619, 0.1792
resid. el. dens. [e·Å^{-3}]	1.446/−1.041	1.162/−1.008	0.690/−0.574	0.783/−0.443	1.272/−1.036

0.7346) and **6b** ($T_{max/min}$ = 1/0.7489) [28]. Crystals of **7** were racemically twinned (ratio of the two twin components 0.533(7):0.467(3)) and one of the $CF_3SO_3^-$ anions was disordered (occupancy factors: 0.912(2) and 0.088(2)). The carbon atom of the CH_2Cl_2 solvent molecule in **9** was found to be disordered about two positions (occupancy factor for both positions: 0.50(3)).

CCDC-617183 (**5a**), -617184 (**6a**), -617185 (**6b**), -617186 (**7**), and -619359 (**9**) contain the supplementary crystallographic data for this paper. These data can be obtained free of charge via www.ccdc.cam.ac.uk/conts/retrieving.html (or from the Cambridge Crystallographic Data Centre, 12 Union Road, Cambridge CB2 1EZ, UK; fax: +44 1223 336 033; deposit@ccdc.cam.uk.

Acknowledgement

We thank José Antonio Cuesta-Seijo, Dr. Mathias Noltemeyer, Thomas Labahn, Denis Vidovic (Göttingen) and Hans Pritzkow (Heidelberg) for collecting the X-ray data. Financial support by the DFG (Me1313/7-1) is gratefully acknowledged.

References

[1] (a) E.I. Solomon, P. Chen, M. Metz, S.-K. Lee, A.E. Palmer, Angew. Chem. 113 (2001) 4702; Angew. Chem. Int. Ed. Engl. 40 (2001) 4570;
(b) L.Q. Hatcher, K.D. Karlin, J. Biol. Inorg. Chem. 9 (2004) 669;
(c) M.A. Halcrow, P.F. Knowles, S.E.V. Phillips, in: I. Bertini, A. Sigel, H. Sigel (Eds.), Handbook on Metalloproteins, Marcel Dekker, 2001, p. 709 (Chapter 15).

[2] C. Eicken, C. Gerdemann, B. Krebs, in: A. Messerschmidt, R. Huber, T. Poulos, K. Wieghardt (Eds.), Handbook of Metalloproteins, vol. 2, Wiley, 2001, p. 1319.

[3] T. Klabunde, C. Eicken, J.C. Sacchettini, B. Krebs, Nat. Struct. Biol. 5 (1998) 1084.

[4] C. Eicken, B. Krebs, J.C. Sacchettini, Curr. Opin. Struct. Biol. 9 (1999) 677.

[5] E.I. Solomon, U.M. Sundaram, T.E. Machonkin, Chem. Rev. 96 (1996) 2563.

[6] I.A. Koval, P. Gamez, C. Belle, K. Selmeczi, J. Reedijk, Chem. Soc. Rev. 35 (2006) 814.

[7] P.E.M. Siegbahn, J. Biol. Inorg. Chem. 9 (2004) 577.

[8] (a) M. Fontecave, J.-L. Pierre, Coord. Chem. Rev. 170 (1998) 125;
(b) A.G. Blackman, W.B. Tolman, Struct. Bonding 97 (2000) 179;
(c) V. Mahadevan, R.J.M. Klein Gebbink, T.D.P. Stack, Curr. Opin. Chem. Biol. 4 (2000) 228.

[9] R.N. Mukherjee, Proc. Indian Natl Sci. Acad. 70 (2004) 329.

[10] (a) N. Oishi, Y. Nishida, K. Ida, S. Kida, Bull. Chem. Soc. Jpn 53 (1980) 2847;
(b) J. Mukherjee, R. Mukherjee, Inorg. Chim. Acta 337 (2002) 429.

[11] C.-H. Kao, H.-H. Wei, Y.-H. Liu, G.-H. Lee, Y. Wang, C.-J. Lee, J. Inorg. Biochem. 84 (2001) 171.

[12] J. Ackermann, F. Meyer, E. Kaifer, H. Pritzkow, Chem.–Eur. J. 8 (2002) 247.

[13] (a) S. Torelli, C. Belle, I. Gautier-Luneau, J.-L. Pierre, E. Saint-Aman, J.-M. Latour, L. Le Pape, D. Luneau, Inorg. Chem. 39 (2000) 3526;
(b) C. Belle, C. Beguin, I. Gautier-Luneau, S. Hamman, C. Philouze, J.-L. Pierre, F. Thomas, S. Torelli, E. Saint-Aman, M. Bonin, Inorg. Chem. 41 (2002) 479.

[14] (a) J. Reim, B. Krebs, J. Chem. Soc., Dalton Trans. (1997) 3793;
(b) J. Anekwe, A. Hammerschmidt, A. Rompel, B. Krebs, Z. Anorg. Allg. Chem. 632 (2006) 1057.

[15] (a) A. Neves, L.M. Rossi, A.J. Bortoluzzi, B. Szpoganicz, C. Wiezbicki, E. Schwingel, W. Haase, S. Ostrovsky, Inorg. Chem. 41 (2002) 1788;
(b) I.A. Koval, M. Huisman, A.F. Stassen, P. Gamez, O. Roubeau, C. Belle, J.-L. Pierre, E. Saint-Aman, M. Luken, B. Krebs, M. Lutz, A.L. Spek, J. Reedijk, Eur. J. Inorg. Chem. (2004) 4036.

[16] M. Merkel, N. Möller, M. Piacenza, S. Grimme, A. Rompel, B. Krebs, Chem.–Eur. J. 11 (2005) 1201.

[17] M. Thirumavalavan, P. Akilan, M. Kandaswamy, K. Chinnakali, G. Senthil Kumar, H.K. Fun, Inorg. Chem. 42 (2003) 3308.

[18] C. Fernandes, A. Neves, A.J. Bortoluzzi, A.S. Mangrich, E. Rentschler, B. Szpoganicz, E. Schwingel, Inorg. Chim. Acta 320 (2001) 12.

[19] S. Torelli, C. Belle, S. Hamman, J.-L. Pierre, E. Saint-Aman, Inorg. Chem. 41 (2002) 3983.

[20] (a) E. Monzani, L. Quinti, A. Perotti, L. Casella, M. Gulotti, L. Randaccio, S. Geremia, G. Nardin, P. Faleschini, G. Tabbi, Inorg. Chem. 37 (1998) 553;
(b) G. Battaini, L. Casella, M. Gullotti, E. Monzani, G. Nardin, A. Perotti, L. Randaccio, L. Santagostini, F.W. Heinemann, S. Schindler, Eur. J. Inorg. Chem. (2003) 1197.

[21] E. Monzani, G. Battaini, A. Perotti, L. Casella, M. Gullotti, L. Santagostini, G. Nardin, L. Randaccio, S. Geremia, P. Zanello, G. Opromolla, Inorg. Chem. 38 (1999) 5359.

[22] M.R. Malachowski, Inorg. Chim. Acta 162 (1989) 199.

[23] (a) F. Meyer, S. Beyreuther, K. Heinze, L. Zsolnai, Chem. Ber./Recueil 130 (1997) 605;
(b) F. Meyer, K. Heinze, B. Nuber, L. Zsolnai, J. Chem. Soc., Dalton Trans. (1998) 207;
(c) M. Konrad, F. Meyer, K. Heinze, L. Zsolnai, J. Chem. Soc., Dalton Trans. (1998) 199;
(d) F. Meyer, P. Rutsch, Chem. Commun. (1998) 1037;
(e) F. Meyer, E. Kaifer, P. Kircher, K. Heinze, H. Pritzkow, Chem.–Eur. J. 5 (1999) 1617;
(f) M. Konrad, F. Meyer, A. Jacobi, P. Kircher, P. Rutsch, L. Zsolnai, Inorg. Chem. 38 (1999) 4559;
(g) B. Bauer-Siebenlist, F. Meyer, E. Farkas, D. Vidovic, J.A.C. Seijo, R. Herbst-Irmer, H. Pritzkow, Inorg. Chem. 43 (2004) 4189;
(h) B. Bauer-Siebenlist, F. Meyer, E. Farkas, D. Vidovic, S. Dechert, Chem.–Eur. J. 11 (2005) 4349.

[24] S. Buchler, F. Meyer, E. Kaifer, H. Pritzkow, Inorg. Chim. Acta 337 (2002) 371.

[25] J. Ackermann, F. Meyer, H. Pritzkow, Inorg. Chim. Acta 357 (2004) 3703.

[26] A.W. Addison, T.N. Rao, J. Reedijk, J. van Rijn, G.C. Verschoor, J. Chem. Soc., Dalton Trans. (1984) 1349.

[27] G.M. Sheldrick, SHELX-97, Programs for Crystal Structure Solution and Refinement, University of Göttingen, Germany, 1997.

[28] G.M. Sheldrick, SADABS, Program for Empirical Absorption Correction of Area Detector Data, University of Göttingen, Germany, 1997.